Nano Research Energy

ISSN 2791-0091 (print); 2790-8119 (online)
https://doi.org/10.26599/NRE.2024.9120143

Research Article

Crystallinity degree of $MoSe_2$ influencing its potassium-ion storage performance

Jiamei Liu[1,2,§], Xiaowei Shi[3,§], Jia Liu[2], Chang Huang[2], Chao Li[4], Haixiao Kang[5] (✉), Zhan Gao[1] (✉), and Lei Li[3] (✉)

[1] *School of Chemical Engineering and Technology, Xi'an Jiaotong University, No.28, Xianning West Road, Xi'an 710049, China*
[2] *Instrument Analysis Center of Xi'an Jiaotong University, Xi'an Jiaotong University, No.28, Xianning West Road, Xi'an 710049, China*
[3] *State Key Laboratory for Mechanical Behavior of Materials, School of Materials Science and Engineering, Xi'an Jiaotong University, No.28, Xianning West Road, Xi'an 710049, China*
[4] *School of Chemistry, Xi'an Jiaotong University, No.28, Xianning West Road, Xi'an 710049, China*
[5] *College of Geography and Environment, Baoji University of Arts and Sciences, Baoji 721013, China*
[§] *Jiamei Liu and Xiaowei Shi contributed equally to this work.*

Received: 24 September 2024 / **Revised:** 20 October 2024 / **Accepted:** 29 October 2024

ABSTRACT

The effect of crystallinity degree of $MoSe_2$ on the potassium ions storage performance in potassium-ion batteries (PIBs) has been largely overlooked in the energy communities. In this study, we experimentally realize $MoSe_2$ grown on graphene nanoribbons ($MoSe_2$-GNR) with tunable crystallinity by tailoring the thermal annealing temperature, and further investigate the effect of crystallinity degree in $MoSe_2$-GNR on the potassium ions storage performance. The spectral, electrochemical, and microscopy experiments indicate that high-temperature thermal annealing results in a high crystallinity degree of $MoSe_2$-GNR with decreased interlayer spacing of (002). The $MoSe_2$-GNR with high crystallinity degree exhibits a high capacity, but suffers from reduced cycling stability. What is more, the *in-situ* X-ray powder diffractometer (*in-situ* XRD) and *in-situ* Raman experiments reveal the phase transition in $MoSe_2$ triggered by potassium ions insertion/extraction during the potassium ions storage. The work sheds light on the development of $MoSe_2$-based anode materials for PIBs.

KEYWORDS

crystallinity degree, potassium ions storage, interlayer spacing, $MoSe_2$

1 Introduction

Potassium-ion batteries (PIBs) are emerging as next-generation energy storage technologies that present viable alternatives to lithium-ion batteries, primarily owing to the relative abundance and cost-effectiveness of potassium [1–4]. The electrochemical performance of PIBs is influenced by many factors, including the electrode materials, the electrolyte, binders, and conductive additives [5–8]. Previous studies have shown that the larger ionic radius of K^+ (1.38 Å) compared to that of Li^+ (0.76 Å) results in elevated diffusion barriers and slower insertion/extraction kinetics, which in turn contribute to the suboptimal electrochemical performance of PIBs [9–15]. Therefore, the exploration of anode materials with appropriately designed interlayer spacing that facilitates efficient K^+ intercalation and deintercalation is essential for advancing the development of PIBs [16, 17]. Among the various potential anode materials for PIBs, transition metal two-dimensional (2D) materials have garnered significant attention due to their unique structural characteristics, high surface area, and tunable electronic properties that can enhance the kinetics of potassium ion transport and improve overall battery performance [9, 17–19]. Molybdenum diselenide ($MoSe_2$), a representative 2D transition-metal dichalcogenides (TMDs), emerges as a promising anode candidate due to its larger interlayer spacing and superior electrical conductivity [20–24]. One significant research direction regarding $MoSe_2$-based anode materials involves the optimization of their structure, including the modification of size and morphology, to enhance the exposure of active sites and achieve superior electrochemical performance, particularly in terms of capacity [25–30]. Additionally, another avenue includes the fabrication of composites that integrate $MoSe_2$ with other electrically conductive materials, which can improve the overall electrical conductivity of the anode [31–38]. These strategies have substantially contributed to the advancement of $MoSe_2$-based anode materials for PIBs. However, the impact of the degree of crystallinity of $MoSe_2$ on electrochemical performance has been largely overlooked by the energy storage research community. Investigating this relationship could provide valuable insights for the further advancement of this field.

Address correspondence to Haixiao Kang, hx_kang@126.com; Zhan Gao, zhangao18@xjtu.edu.cn; Lei Li, l-li@xjtu.edu.cn

Here, we tune the crystallinity of $MoSe_2$ grown on graphene nanoribbons ($MoSe_2$-GNR) via tailoring the thermal annealing temperature and study its effect on the electrochemical performance as anode in PIBs. The spectral and microscopy experiments indicated that the increase of thermal annealing temperature results in the increase of crystallinity degree of $MoSe_2$-GNR, along with the decrease of its interlayer spacing of (002). The crystallinity degree of $MoSe_2$-GNR greatly influenced its electrochemical performance in PIBs. The increase of crystallinity degree of $MoSe_2$-GNR leaded to high capacity, but reduced cycling stability. Beyond this, the *in-situ* Raman and *in-situ* X-ray powder diffractometer (*in-situ* XRD) were carried out to explore the K^+ storage mechanism in $MoSe_2$-GNR, revealing a phase transition in $MoSe_2$ triggered by the insertion and extraction of K^+ ions. The work presented here would be beneficial for the development of $MoSe_2$-based anode materials for PIBs.

2 Experimental

2.1 Synthesis of $MoSe_2$-GNR

Graphene nanoribbons (GNR) were synthesized following a previously reported method [39, 40], serving as the substrates for $MoSe_2$ loading. The $MoSe_2$-GNR was synthesized through a hydrothermal reaction. 100 mg of GNR was ultrasonically dispersed in 200 mL of 5 mol·L^{-1} HNO_3 for 10 min, followed by reflux heating at 100 ℃ for 18 h. The resulting product was washed three times with deionized water (Hitech, Master-S15) to a neutral pH value of 7. 1 mmol of Se powder (Aladdin, 99.99%) was completely dissolved in 10 mL of $N_2H_4{\cdot}H_2O$ (National Pharmaceutical Group, 85%) solution to yield the Se $N_2H_4{\cdot}H_2O$ mixture solution. 25 mg of activation treated GNR was ultrasonically dispersed in 30 mL of deionized water, followed by the sequential addition of 0.5 mmol of $Na_2MoO_4{\cdot}2H_2O$ (Aladdin, 99.0%) and the aforementioned Se/$N_2H_4{\cdot}H_2O$ solution. After stirring for 1 h, the suspension was transferred to a 100 mL Teflon-lined stainless-steel autoclave and subjected to a 12-hour reaction at 200 ℃. The resulting product underwent thorough 5 times washing with deionized water and anhydrous ethanol (National Pharmaceutical Group, 99.7%), respectively. The product was dried at 60 ℃ for 12 h and annealed for 10 h at different temperatures (600 ℃, 700 ℃, and 800 ℃) in an Argon atmosphere. The product was named as MG-X, in which M stands for $MoSe_2$, G stands for GNR, and X stands for the annealing temperature.

2.2 Preparation of electrodes

MG-X electrodes were fabricated by coating a mixed slurry of MG-X, conductive additive (Timical Super C65, MTI Corp.), and binder (PVDF, HSV900, MTI Corp.) in a weight ratio of 7:2:1 in NMP (Aladdin, >99.9%) onto Cu foil current collectors. The coated electrodes were dried at 100 ℃ for 10 h under vacuum conditions. The resulting electrodes have an approximate active material mass loading of ~ 1.7 mg·cm^{-2}.

2.3 Preparation of the battery

The battery was assembled on a CR2032 coin-type battery in an argon-filled glovebox (Universal, Mikrouna), where the concentration of both H_2O and O_2 was maintained below 0.1 ppm. Within the half-battery PIBs, MG-X electrode operated as the anode, K foil functioned as the cathode, a glass fiber was used as separator, and the electrolyte was consisted of 1 mol·L^{-1} potassium difluorosulfonimide (KFSI) in a solvent mixture of diethyl carbonate and ethylene carbonate (1:1 by volume).

2.4 Materials characterization

X-ray diffraction (XRD) analysis was conducted using a Bruker D8-Advance X-ray diffractometer equipped with Cu-Kα radiation (λ =1.5418 Å). Raman spectroscopy measurements were carried out utilizing a HORIBA LabRAM HR Evolution spectrometer. The morphologies of the materials were examined using field emission scanning electron microscopy (FESEM, Zeiss Gemini 500) and transmission electron microscopy (TEM, JEOL JEM-F200). X-ray photoelectron spectroscopy (XPS) data was acquired with a ThermoFisher ESCALAB Xi+ spectrometer utilizing monochromatic Al Kα X-ray radiation. Thermal gravimetric (TG) analysis was performed using a Synchronous thermal analyzer (TG-DSC, METTLER TOLEDO TGA/DSC 3+).

2.5 Electrochemical evaluation of batteries

Cyclic voltammetry (CV) measurements were conducted on an AMETEK ParSTAT MC (PMCCHS08A) potentiostat. Galvanostatic charge discharge experiments, the rate capability and cycling performance assessments of the batteries, were evaluated using a multichannel battery test system (Land CT 2001A). The specific capacity of the half-battery was determined based on the mass of active material of anode. All electrochemical measurements were performed at room temperature.

3 Results and discussion

Scheme 1 illustrates the synthesis process of MG-X. GNR was prepared from carbon nanotubes (CNT) following a methodology described in the reported literature [39, 40]. The prepared GNR was combined with Na_2MoO_4, Se and $N_2H_4{\cdot}H_2O$ mixed solution in water to prepare the uniform $MoSe_2$ loading onto GNR through hydrothermal reaction. The resulting materials were subjected to annealing in an argon atmosphere, resulting in the formation of MG-X. Regulating the annealing temperature can tuning the interlayer spacing of the (002) plane of $MoSe_2$. The detailed experimental procedure was provided in the experimental section.

The morphologies of MG-X were characterized using FESEM and TEM. Figures 1(a) and 1(b) show the SEM images of MG-600 at different magnifications. It is clearly seen that $MoSe_2$ nanosheets are evenly dispersed on the surface of GNRs. Figures 1(c) and 1(d) show the high-resolution transmission electron microscopy (HRTEM) images of MG-600 at different magnifications. It exhibits clear lattice fringes and layered structure. The interlayer spacing of (002) in MG-600 is 0.670 nm (Fig. 1(d) and Fig. S1(a) in the Electronic Supplementary Material (ESM)). With the increasing annealing temperature, the morphologies of MG-X have a little variation. MG-600 and MG-700 appear similar morphology, while MG-800 has a distinct change in morphology, where $MoSe_2$ nanosheets exhibit certain shrinkage on GNR surface (Figs. 1(e), 1(f), 1(i) and 1(j)).

The interlayer spacing of (002) in MG-700 and MG-800 was 0.666 and 0.653 nm (Figs. 1(h) and 1(l) and Figs. S1(b) and S1(c) in the ESM), respectively. The interlayer spacing of (002) in MG-X decreases with the increase of thermal annealing temperature.

The crystal structure and chemical composition of MG-X were also studied by XRD, Raman, and XPS. As demonstrated in Fig. 2(a) and Table 1, the XRD peaks of MG-X matched well with the

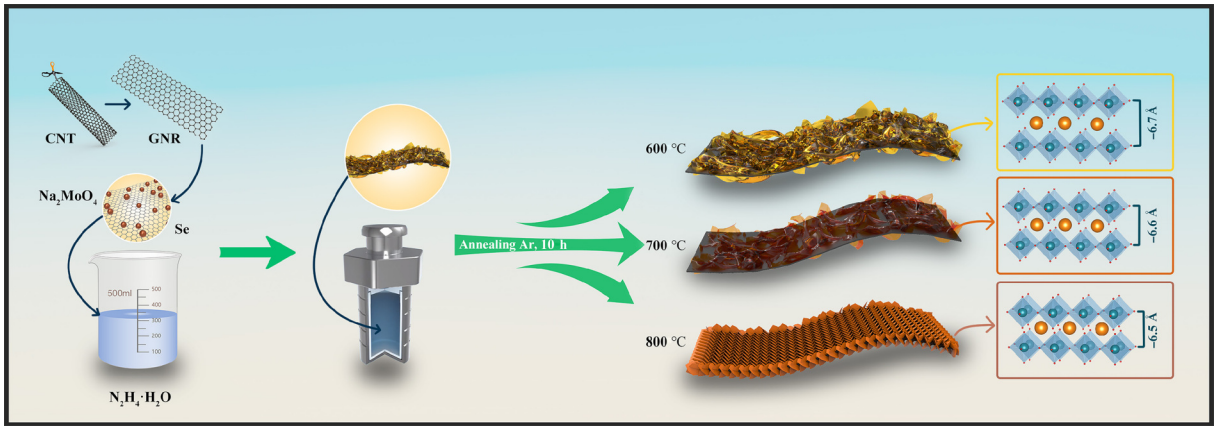

Scheme 1 Schematic illustration of the synthetic process of MG-X.

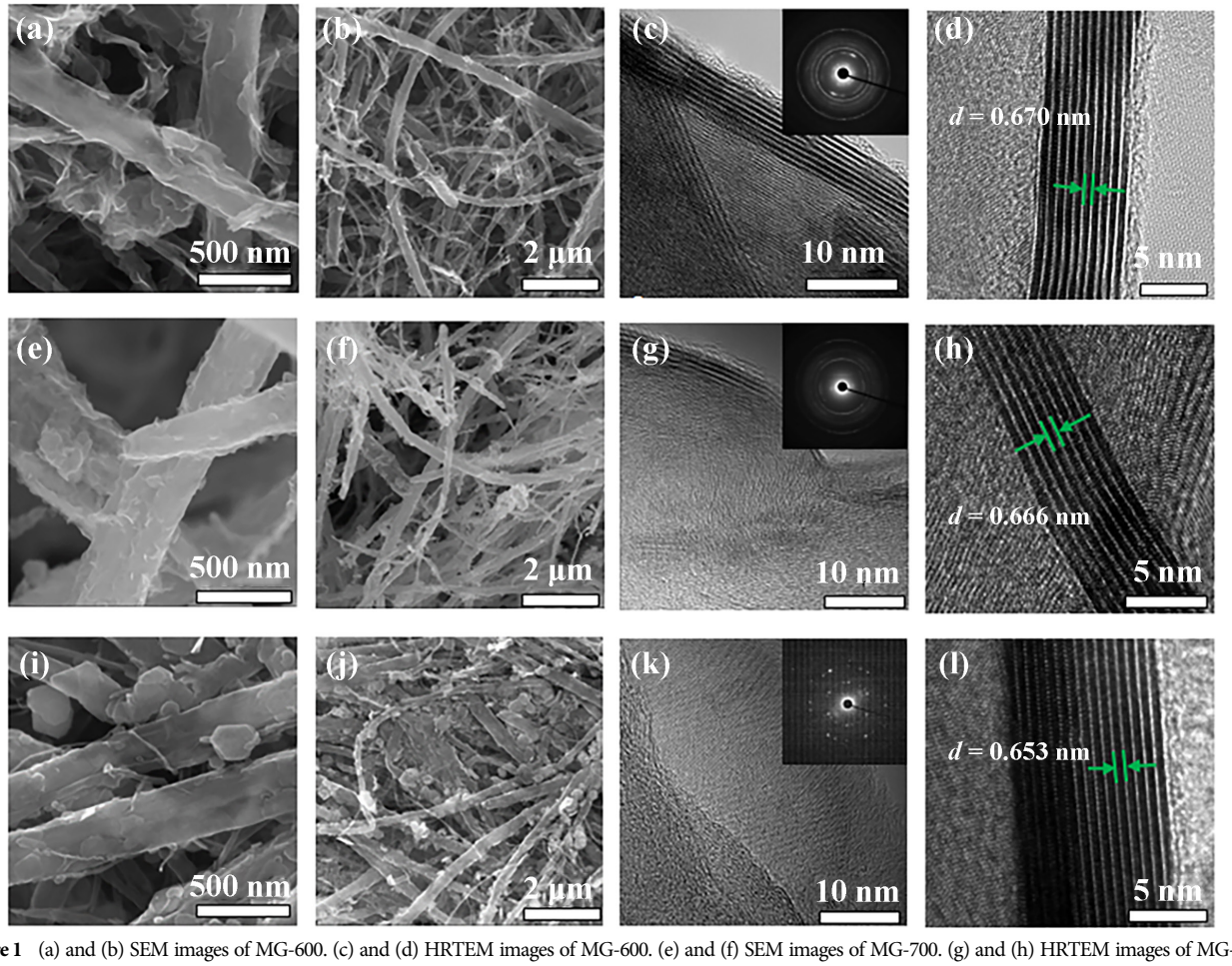

Figure 1 (a) and (b) SEM images of MG-600. (c) and (d) HRTEM images of MG-600. (e) and (f) SEM images of MG-700. (g) and (h) HRTEM images of MG-700. (i) and (j) SEM images of MG-800. (k) and (l) HRTEM images of MG-800.

hexagonal-$MoSe_2$ phase (PDF 04-004-4226), except for the peak at 26.3° attributed to GNR (Fig. S2 in the ESM). Table 1 shows the position of different peaks in MG-X [41, 42]. Obviously, the interlayer spacing of (002) peak in MG-X closely aligned with the HRTEM observations. The peak positions and shapes of (002) and (105) diffraction peaks differed among these three samples. The diffraction peaks of MG-600, MG-700, and MG-800 exhibited varying intensity and shape under different annealing temperature. The increasing annealing temperature results in the sharp shape with high intensity, indicating the high crystallinity. This indicates that MG-800 exhibits the highest degree of crystallinity, followed by MG-700 with intermediate crystallinity, while MG-600 displays the lowest crystallinity among the three samples.

The Raman spectra were examined to investigate the influence of processing temperature on the vibrational structure of MG-X (Fig. 2(b)). The two distinct peaks in MG-X at 237 and 283 cm^{-1} can be assigned to the out-plane Mo-Se phonon mode (A^1_g) and in-plane Mo-Se phonon (E^1_{2g}) of $MoSe_2$, respectively. Compared to pure $MoSe_2$, the intensity ratio of A^1_g / E^1_{2g} is significantly increased in MG-X, indicating a high abundance of edge-terminated structures within the materials [43, 44]. Moreover, an increase in treatment temperature leads to a higher intensity ratio of A^1_g / E^1_{2g}, suggesting that elevated temperatures result in a

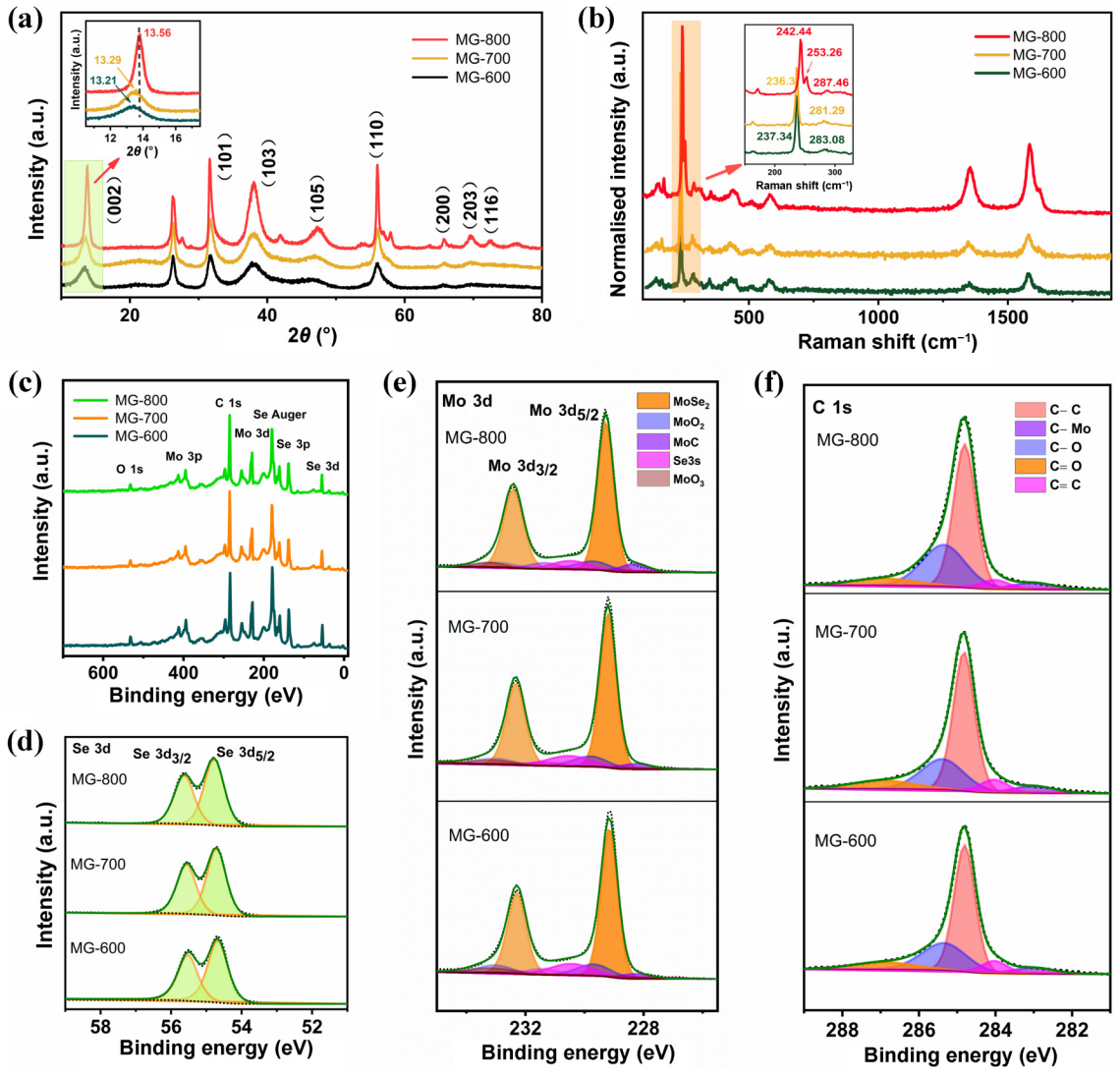

Figure 2 (a) XRD patterns of MG-X. (b) Raman spectra of MG-X. (c) XPS survey of MG-X. (d) Se 3d of MG-X. (e) Mo 3d of MG-X. (f) C 1s of MG-X.

Table 1 The XRD peaks of $MoSe_2$ in MG-600, MG-700, and MG-800

(2θ/°)	002	101	103	105	110	200	203	d(002)/(Å)	d(105)/(Å)
MG-600	13.21	31.51	37.82	45.30	55.83	65.50	69.43	6.70	2.00
MG-700	13.29	31.51	37.82	46.64	55.83	65.50	69.43	6.66	1.95
MG-800	13.56	31.51	37.82	47.12	55.83	65.50	69.43	6.53	1.93

greater presence of edge-terminated structures in MG-X. Notably, MG-800 exhibits a blue-shifted A^1_g peak compared to the other samples, which may be attributed to the increased crystallinity and van der Waals forces between $MoSe_2$ layers under higher temperature treatment conditions. This increase in crystallinity with rising annealing temperature aligns well with the XRD results. Additionally, the peaks at 1347 and 1579 cm^{-1} correspond to typical carbon shifts associated with D-band and G-band vibrations in GNR of MG-X, respectively [41, 43, 45–48].

X-ray photoelectron spectroscopy was also utilized to analyze the interfacial chemical composition and valence states. As shown in Figs. 2(c)–2(f), the survey spectra of MG-X reveal four main elements of Se, Mo, C, and O. The Se 3d spectra were deconvoluted into two peaks located at 54.7 and 55.6 eV, corresponding to the Mo-Se bond (Se^{2-}). The Mo 3d spectra were well resolved into four sets of peaks. The peaks at 228.2 and 231.4 eV assigned to Mo-C bond, the peaks at 229.2 and 232.3 eV assigned to Mo-Se bond, the peaks at 229.8 and 233.1 eV assigned to Mo-O bond (Mo^{4+}), and the peaks at 233.2 and 235.7 eV assigned to Mo-O bond (Mo^{6+}) [49, 50]. The C 1s spectra were deconvoluted into five peaks located at 283.0, 284.0, 284.8, 285.4 and 287.0 eV, assigned to C–Mo, C=C, C–C, C–O, and C=O, respectively [51–53]. The Brunauer–Emmett–Teller (BET) surface area of MG-600, MG-700 and MG-800 is 50.4, 45.2, and 48.3 $m^2 \cdot g^{-1}$, respectively (Fig. S3 in the ESM). The $MoSe_2$ content in MG-600, MG-700, and MG-800 is 63.0, 64.3, and 59.7 wt.%, respectively, based on thermogravimetry (Fig. S4 in the ESM) [26]. All these results indicate that the designed MG-X with different crystallinity were successfully prepared.

The electrochemical performance of MG-X for potassium-ion storage was evaluated using CR2032-type coin batteries. The charge/discharge capacity was determined based on the active

material of MG in MG-X, calculated using TG curves (Fig. S4 in the ESM). The rate performance of MG-X under different current densities from 0.1 to 5.0 A·g^{-1} is shown in Fig. 3(a). The three samples demonstrate obvious difference in capacity at different current densities. MG-800 has high capacity at low current density, but displayed the fastest capacity decay with the increase of current densities. MG-700 has the highest capacity of 421 mAh·g^{-1} at 0.1 A·g^{-1} and a medium capacity decay with the increase of current density compared to MG-600 and MG-800. MG-600 exhibits the lowest capacity at low current density and also demonstrates the slowest capacity decay with increasing current density among all samples.They also demonstrate the high capacity in volumetric metric as shown in Fig. S5 in the ESM.

The long-term cycle performance of MG-X was evaluated at 0.1 A·g^{-1} for the first 10 cycles, followed by subsequent cycles at 2 A·g^{-1}. The capacity retention from the 11th to the 100th cycle is recorded as 90%, 84%, and 76% for MG-600, MG-700, and MG-800, respectively (Fig. 3(b)). The MG-600 with low crystallinity has the best cycling stability among all the samples. The results regarding the capacity, rate and cycling performance indicate that varying crystallinity degree of $MoSe_2$ in MG-X greatly affects their electrochemical performance. The elevated crystallinity of $MoSe_2$ in MG-X frequently results in increased capacity, but diminished rate capability and cycling stability. As a result, MG-800 demonstrates the poorest rate performance and cycling stability, whereas MG-600 showcases the highest cycling stability among the examined samples.

In order to elucidate the impact of $MoSe_2$ morphology on the structural stability of MG-X during the charge/discharge process, HRTEM imaging was performed on the electrodes after 100 cycles. Compared with the original material, a significant change in crystal spacing can be seen in the HRTEM images of MG-600, MG-700, and MG-800 electrodes (Fig. 4 and Fig. S6 in the ESM). The corresponding crystal spacing of (002) in MG-X changes from 0.670, 0.666, and 0.653 nm in MG-600, MG-700, and MG-800 to 0.706, 0.708, and 0.725 nm, respectively. Thus, all these samples exhibit certain degree of volume expansion due to potassium ion insertion. MG-800 exhibits the highest degree of expansion, resulting in the poorest stable performance.

To further elucidate the potassium storage mechanism of the target electrode, *in-situ* Raman spectroscopy and *in-situ* XRD were systematically conducted at different charge/discharge states during the initial cycle. MG-700 was selected as the sample for this study. Figure 5(a) illustrates the *in-situ* Raman spectra obtained during the first potassiation and depotassiation processes in MG-700 (Fig. S7 in the ESM). It exhibits a slight blue shift of peak A^1_g (240 cm^{-1}) compared to *ex-situ* test result (237 cm^{-1}). The characteristic peaks of $MoSe_2$ (A^1_g: 240 cm^{-1} and E^1_{2g}: 283 cm^{-1}) gradually diminish with ongoing discharging, indicating gradual embedding of potassium ions into the interlayer of $MoSe_2$. Upon reaching a discharge voltage of 2.0 V, a fresh peak at 276 cm^{-1} progressively emerges, assigned to K_xSe. All characteristic peaks completely disappear upon fully discharge at 0.01 V. However, upon charging to 3 V, a reversible A^1_g peak at 255 cm^{-1} is detected along with broadening width, suggesting reversible conversion reaction into $MoSe_2$ during both potassiation and depotassiation processes. The results also demonstrate complete expulsion of potassium ions from K_xSe, and converted to $MoSe_2$ and $Mo_{15}Se_{19}$ with Mo. The observed shift is caused by changes in interlayer spacing and the number of layers present within the material structure [31, 54]. This finding is consistent with the observations made in HRTEM analysis described earlier. Additionally, D and G peaks associated with GNR are observed throughout this process. These D and G peaks undergo significant red-shifts accompanied by broadening during discharging due to K^+ embedding within the electrodes [9]. During charging, these characteristic carbon peaks recover their original status, indicating excellent reversibility and stability of GNR in MG-700. As shown in Fig. 5(b), the *in-situ* XRD patterns of MG-700 revealed significant changes in the diffraction peaks of $MoSe_2$ during the charging-discharging process (Fig. S8 in the ESM). Specifically, the (103) peak of MG-700 at ~ 37.8° exhibited a gradual leftward shift during the

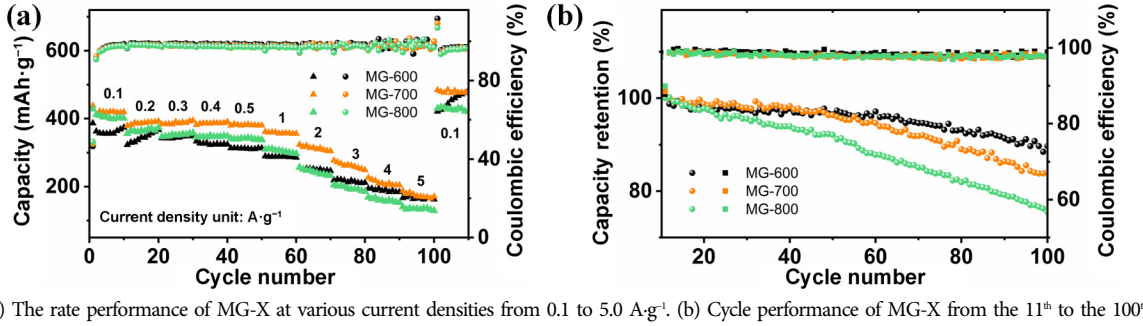

Figure 3 (a) The rate performance of MG-X at various current densities from 0.1 to 5.0 A·g^{-1}. (b) Cycle performance of MG-X from the 11th to the 100th cycle at 2 A·g^{-1}.

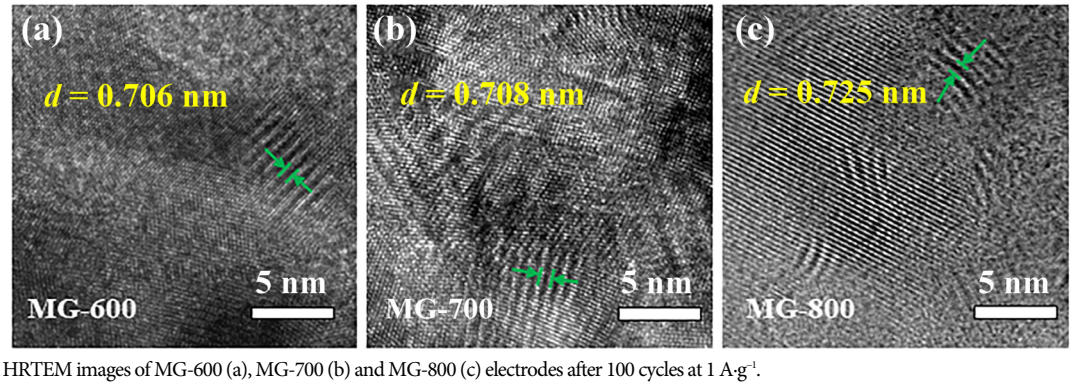

Figure 4 The HRTEM images of MG-600 (a), MG-700 (b) and MG-800 (c) electrodes after 100 cycles at 1 A·g^{-1}.

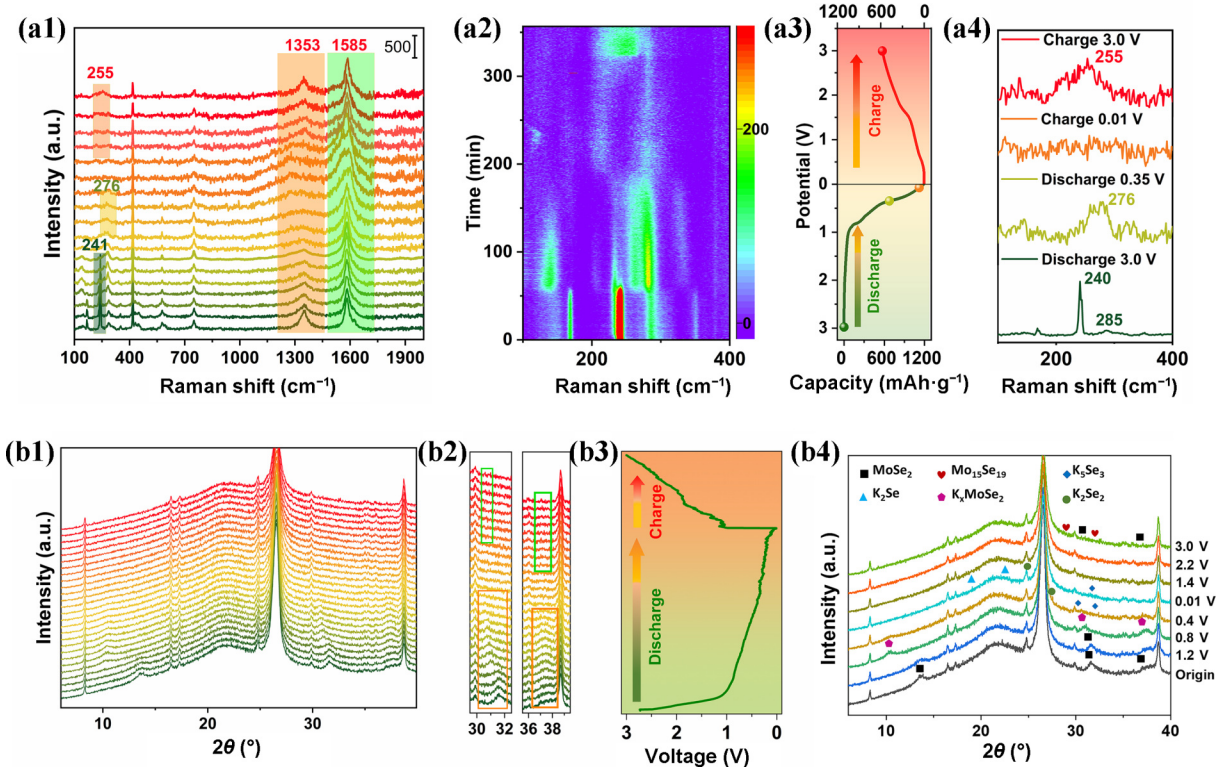

Figure 5 The analysis of potassium ion storage mechanism of MG-700. (a) *In-situ* Raman plots ((a3) shows the initial cycle charge/discharge curve at 0.3 A·g^{-1}). (b) *In-situ* XRD patterns ((b3) shows the initial cycle charge/discharge curve at 0.2 A·g^{-1}).

discharging process and eventually disappeared upon completion of the full discharge cycle. Subsequent to full charging at 3 V, a weak (103) peak gradually reappeared, indicating reversible insertion/deinsertion processes. A similar trend was also observed for the (101) peak at ~ 31.5°, further supporting the reversibility of electrochemical reactions. The crystal phase structure of $MoSe_2$ underwent noticeable changes accompanied by potassium embedding process, confirming alterations in the material composition. Particularly, upon reaching a discharge voltage of 0.8 V, the three peaks of $MoSe_2$, including (002), (101), and (103), gradually shifted to lower angles and weakened, attributed to the intercalation of potassium ions into $MoSe_2$ layers, leading to an increased interlayer spacing and the formation of a highly disordered layered structure. As potassium ions accumulated within the host, an intermediate transition phase of K_xMoSe_2 began to appear. Upon discharging to 0.4 V, the characteristic peaks corresponding to K_5Se_3 at 30.8° and 32.2°, and K_2Se_2 at 24.8° and 27.4° emerged due to electrochemical reactions, transforming K_xMoSe_2 to K_xSe. In the first fully discharged state, at a voltage level as low as 0.01 V, all typical peaks associated with $MoSe_2$ completely disappeared, instead corresponding characteristic peaks related to K_2Se, K_2Se_2, and K_5Se_3 appeared. In the subsequent charging process, the characteristic peaks associated with K_2Se, K_2Se_2, and K_5Se_3 gradually became weakened due to electrochemical reactions between Mo and K_xSe, giving rise to Mo_xSe_y. With charging up to 3 V, peaks of $Mo_{15}Se_{19}$ and $MoSe_2$ emerged [9, 31, 38]. Interestingly, the (002) peak at ~13.3° also exhibited a leftwards shift during discharging. In contrast to the previously mentioned peaks, it did not reappear after charging to 3 V. Additionally, the presence of a peak at 38.5° corresponding to BeO, originating from the *in-situ* cell setup, was noted. Based on the comprehensive analysis of the experimental results, a plausible potassium storage mechanism in $MoSe_2$ can be proposed as reaction 1 ($MoSe_2 + xK^+ + xe^- \leftrightarrow K_xMoSe_2$) and reaction 2 ($3K_xMoSe_2 + (10 - 3x)\ K^+ + (10 - 3x)\ e^- \leftrightarrow 2K_5Se_3 + 3Mo$) [9, 55, 56].

Cyclic voltammetry testing was employed to further confirm the electrochemical mechanisms governing potassium ion intercalation and deintercalation in MG-700, as illustrated in Fig. S9 in the ESM. During the initial charge process, the reduction peaks at 0.34 and 0.57 V are attributed to the reduction of K_xMoSe_2 into Mo and K_2Se, as well as the formation of solid electrolyte interphase (SEI). Furthermore, the peak at 1.82 V corresponds to the highly reversible depotassiation process, with the corresponding oxidation peak at 1.11 V in the subsequent discharge process [41, 54, 57]. Subsequent cycles exhibit well-overlapping CV curves with the initial charge and discharge processes, albeit with minor peak position variations, underscoring the remarkable electrochemical stability and reversibility of MG-700. The findings from *in-situ* XRD and *in-situ* Raman spectroscopy experiments are in good agreement with those from the CV analysis.

4 Conclusions

In conclusion, we have synthesized MG-X with tunable degrees of crystallinity. When evaluated as the anode material for PIBs, MG-X with high crystallinity exhibited high capacity, but limited cycling stability due to the reduced structural integrity upon cycling, notable changes in crystal plane spacing. MG-700 demonstrated comprehensive potassium storage ability, including a high specific capacity of 421 mAh·g^{-1} at 0.1 A·g^{-1}, good rate, and cycling stability. Through comprehensive analysis employing *in-situ* XRD, *in-situ* Raman spectroscopy, and HRTEM, we elucidated the underlying reaction mechanism between $MoSe_2$ and potassium, identifying the principal discharge products as

K_2Se, K_2Se_2, and K_5Se_3, while the charge products comprised $MoSe_2$ and $Mo_{15}Se_{19}$. This study provides valuable insights for the development of innovative negative electrode materials for PIBs.

Acknowledgements

This work was supported by the Innovation Capability Support Program of Shaanxi (No. 2024CX-GXPT-12).

Electronic Supplementary Material: Supplementary material (XRD patterns of GNR, HRTEM images of samples, TGA and BET curves of MG-X, CV curves of MG-700, and HRTEM images of cycled electrodes) is available in the online version of this article at https://doi.org/10.26599/NRE.2024.9120143.

Declaration of conflicting interests

The authors declare no conflicting interests regarding the content of this article.

Data availability

All data needed to support the conclusions in the paper are presented in the manuscript and/or the Supplementary Materials. Additional data related to this paper may be requested from the corresponding author upon request.

References

[1] Armand, M.; Tarascon, J. M. Building better batteries. *Nature* **2008**, *451*, 652–657.

[2] Jiang, M. X.; Hu, Y. J.; Mao, B. G.; Wang, Y. X.; Yang, Z.; Meng, T.; Wang, X.; Cao, M. H. Strain-regulated Gibbs free energy enables reversible redox chemistry of chalcogenides for sodium ion batteries. *Nat. Commun.* **2022**, *13*, 5588.

[3] Wang, Z. H.; Feng, X.; Bai, Y.; Yang, H. Y.; Dong, R. Q.; Wang, X. R.; Xu, H. J.; Wang, Q. Y.; Li, H.; Gao, H. C. et al. Probing the energy storage mechanism of quasi-metallic Na in hard carbon for sodium-ion batteries. *Adv. Energy Mater.* **2021**, *11*, 2003854.

[4] Wang, S. J.; Zhao, S.; Guo, X.; Wang, G. X. 2D material-based heterostructures for rechargeable batteries. *Adv. Energy Mater.* **2022**, *12*, 2100864.

[5] Li, J. F.; Fu, H. W.; Gu, M. Y.; Chen, J.; Zhou, J.; Fan, L.; Lu, B. A. Ether-based gel polymer electrolyte for high-voltage potassium ion batteries. *Nano Lett.* **2024**, *24*, 11419–11428.

[6] Zhang, C. L.; Zhao, H. P.; Lei, Y. Recent research progress of anode materials for potassium-ion batteries. *Energy Environ. Mater.* **2020**, *3*, 105–120.

[7] Hosaka, T.; Kubota, K.; Hameed, A. S.; Komaba, S. Research development on K-ion batteries. *Chem. Rev.* **2020**, *120*, 6358–6466.

[8] Qu, Z. X.; Zhang, X. X.; Huang, R. L.; Wu, S. M.; Chen, R. J.; Wu, F.; Li, L. Ultrastable bioderived organic anode induced by synergistic coupling of binder/carbon-network for advanced potassium-ion storage. *Nano Lett.* **2022**, *22*, 4115–4123.

[9] Ge, J. M.; Fan, L.; Wang, J.; Zhang, Q. F.; Liu, Z. M.; Zhang, E. J.; Liu, Q.; Yu, X. Z.; Lu, B. A. $MoSe_2$/N-doped carbon as anodes for potassium-ion batteries. *Adv. Energy Mater.* **2018**, *8*, 1801477.

[10] Feng, W. T.; Feng, N. Y.; Liu, W.; Cui, Y. P.; Chen, C.; Dong, T. T.; Liu, S.; Deng, W. Q.; Wang, H. L.; Jin, Y. C. Liquid-state templates for constructing B, N, co-doping porous carbons with a boosting of potassium-ion storage performance. *Adv. Energy Mater.* **2021**, *11*, 2003215.

[11] Qin, G. H.; Liu, Y. H.; Liu, F. S.; Sun, X.; Hou, L. R.; Liu, B. B.; Yuan, C. Z. Magnetic field assisted construction of hollow red P nanospheres confined in hierarchical N-doped carbon nanosheets/nanotubes 3D framework for efficient potassium storage. *Adv. Energy Mater.* **2021**, *11*, 2003429.

[12] Zhou, L.; Cao, Z.; Zhang, J.; Cheng, H.; Liu, G.; Park, G. T.; Cavallo, L.; Wang, L. M.; Alshareef, H. N.; Sun, Y. K. et al. Electrolyte-mediated stabilization of high-capacity micro-sized antimony anodes for potassium-ion batteries. *Adv. Mater.* **2021**, *33*, 2005993.

[13] Zhang, S. P.; Ling, F. X.; Wang, L. F.; Xu, R.; Ma, M. Z.; Cheng, X. L.; Bai, R. L.; Shao, Y.; Huang, H. J.; Li, D. J. et al. An open-ended Ni_3S_2-Co_9S_8 heterostructures nanocage anode with enhanced reaction kinetics for superior potassium-ion batteries. *Adv. Mater.* **2022**, *34*, 2201420.

[14] Xu, Y. N.; Liu, X. F.; Su, H.; Jiang, S.; Zhang, J. M.; Li, D. Hierarchical bimetallic selenides $CoSe_2$–$MoSe_2$/rGO for sodium/potassium-ion batteries anode: Insights into the intercalation and conversion mechanism. *Energy Environ. Mater.* **2022**, *5*, 627–636.

[15] Luo, B.; Wu, P.; Zhang, J. F.; Cao, L.; Wang, C. H.; Lu, B.; Zhang, B.; Ou, X. van der Waals heterostructure engineering by 2D space-confinement for advanced potassium-ion storage. *Nano Res.* **2021**, *14*, 3854–3863.

[16] Li, Z. W.; Han, M. S.; Zhang, Y. B.; Yuan, F.; Fu, Y.; Yu, J. Single-layered MoS_2 fabricated by charge-driven interlayer expansion for superior lithium/sodium/potassium-ion-battery anodes. *Adv. Sci.* **2023**, *10*, 2207234.

[17] Di, S. J.; Ding, P.; Wang, Y. Y.; Wu, Y. L.; Deng, J.; Jia, L.; Li, Y. G. Interlayer-expanded MoS_2 assemblies for enhanced electrochemical storage of potassium ions. *Nano Res.* **2020**, *13*, 225–230.

[18] Zhang, R. D.; Bao, J. Z.; Pan, Y. L.; Sun, C. F. Highly reversible potassium-ion intercalation in tungsten disulfide. *Chem. Sci.* **2019**, *10*, 2604–2612.

[19] Ren, X. D.; Zhao, Q.; Mcculloch, W. D.; Wu, Y. Y. MoS_2 as a long-life host material for potassium ion intercalation. *Nano Res.* **2017**, *10*, 1313–1321.

[20] Javed, S.; Suo, G. Q.; Mu, R. R.; Lin, C. J.; Li, J. R. Progress and strategies in transition metal chalcogenides as anode for potassium-ion batteries. *J. Energy Storage* **2024**, *97*, 112781.

[21] Ali, Z.; Zhang, T.; Asif, M.; Zhao, L. N.; Yu, Y.; Hou, Y. L. Transition metal chalcogenide anodes for sodium storage. *Mater. Today* **2020**, *35*, 131–167.

[22] Peng, Y.; Wei, M. X.; Zhang, D.; Liu, X.; Xiong, X. S.; Gao, W. J.; Fan, W. J.; Yang, H. Y.; Zhou, Q.; Wang, T. et al. Recent advances in metal selenides as advanced anode materials for potassium-ion batteries. *Nano Energy* **2024**, *130*, 110077.

[23] Lin, H. Z.; Li, M. L.; Yang, X.; Yu, D. X.; Zeng, Y.; Wang, C. Z.; Chen, G.; Du, F. Nanosheets-assembled CuSe crystal pillar as a stable and high-power anode for sodium-ion and potassium-ion batteries. *Adv. Energy Mater.* **2019**, *9*, 1900323.

[24] Li, J. J.; Zhang, W.; Zheng, W. T. Metal selenides find plenty of space in architecting advanced sodium/potassium ion batteries. *Small* **2024**, *20*, 2305021.

[25] Chong, S. K.; Wei, X. D.; Wu, Y. F.; Sun, L.; Shu, C. Y.; Lu, Q. B.; Hu, Y. Z.; Cao, G. Z.; Huang, W. Expanded $MoSe_2$ nanosheets vertically bonded on reduced graphene oxide for sodium and potassium-ion storage. *ACS Appl. Mater. Interfaces* **2021**, *13*, 13158–13169.

[26] Yousaf, M.; Wang, Y. S.; Chen, Y. J.; Wang, Z. P.; Firdous, A.; Ali, Z.; Mahmood, N.; Zou, R. Q.; Guo, S. J.; Han, R. P. S. A 3D trilayered CNT/$MoSe_2$/C heterostructure with an expanded $MoSe_2$ interlayer spacing for an efficient sodium storage. *Adv. Energy Mater.* **2019**, *9*, 1900567.

[27] Li, Y.; Han, M. S.; Zhou, Z. H.; Xia, X. H.; Chen, Q. G.; Chen, M. H. Topological insulator-assisted $MoSe_2$/Bi_2Se_3 heterostructure: Achieving fast reaction kinetics toward high rate sodium-ion batteries. *ChemElectroChem* **2021**, *8*, 697–704.

[28] Lee, J. S.; Park, J. S.; Baek, K. W.; Saroha, R.; Yang, S. H.; Kang, Y. C.; Cho, J. S. Coral-like porous microspheres comprising

polydopamine-derived N-doped C-coated $MoSe_2$ nanosheets composited with graphitic carbon as anodes for high-rate sodium- and potassium-ion batteries. *Chem. Eng. J.* **2023**, *456*, 141118.

[29] Li, J.; Hu, H. X.; Qin, F. R.; Zhang, P.; Zou, L.; Wang, H. B.; Zhang, K.; Lai, Y. Q. Flower-like $MoSe_2$/C composite with expanded (002) planes of few-layer $MoSe_2$ as the anode for high-performance sodium-ion batteries. *Chem. Eur. J.* **2017**, *23*, 14004–14010.

[30] Feng, W. T.; Wei, X. R.; Cao, F. L.; Li, Y. T.; Zhang, X. H.; Li, Y. P.; Liu, W.; Han, J. W.; Kong, D. B.; Zhi, L. J. Defective MoSSe with local-expanded structure for high-rate potassium ion battery. *Energy Storage Mater.* **2024**, *65*, 103186.

[31] Zhong, F. L.; Xu, A. D.; Zeng, Q.; Wang, Y. J.; Li, G. L.; Xu, Z. G.; Yan, Y. R.; Wu, S. P. Confining $MoSe_2$ nanosheets into N-doped hollow porous carbon microspheres for fast-charged and long-life potassium-ion storage. *ACS Appl. Mater. Interfaces* **2021**, *13*, 59882–59891.

[32] Huang, H. W.; Cui, J.; Liu, G. X.; Bi, R.; Zhang, L. Carbon-coated $MoSe_2$/MXene hybrid nanosheets for superior potassium storage. *ACS Nano* **2019**, *13*, 3448–3456.

[33] Park, G. D.; Park, J. S.; Kim, J. K.; Kang, Y. C. Recent advances in heterostructured anode materials with multiple anions for advanced alkali-ion batteries. *Adv. Energy Mater.* **2021**, *11*, 2003058.

[34] Ge, P.; Zhang, L. M.; Yang, Y.; Sun, W.; Hu, Y. H.; Ji, X. B. Advanced $MoSe_2$/carbon electrodes in Li/Na-ions batteries. *Adv. Mater. Interfaces* **2020**, *7*, 1901651.

[35] Wang, Y. Y.; Kang, W. P.; Wei, X. F.; Lu, X. Q.; Sun, D. F. Seed-induced strategy for the construction of nitrogen-doped carbon coated $MoSe_2$/ZnSe-NC nanotubes with enriched phase boundaries toward boosting Na/K-ion storage. *Chem. Eng. J.* **2024**, *482*, 148927.

[36] Zeng, L. X.; Kang, B. Y.; Luo, F. Q.; Fang, Y. X.; Zheng, C.; Liu, J. B.; Liu, R. P.; Li, X. Y.; Chen, Q. H.; Wei, M. D. et al. Facile synthesis of ultra-small few-layer nanostructured $MoSe_2$ embedded on N, P co-doped bio-carbon for high-performance half/full sodium-ion and potassium-ion batteries. *Chem. Eur. J.* **2019**, *25*, 13411–13421.

[37] Zhao, Y.; Sun, Z. T.; Yi, Y. Y.; Lu, C.; Wang, M. L.; Xia, Z.; Lian, X. Y.; Liu, Z. F.; Sun, J. Y. Precise synthesis of N-doped graphitic carbon via chemical vapor deposition to unravel the dopant functions on potassium storage toward practical K-ion batteries. *Nano Res.* **2021**, *14*, 1413–1420.

[38] Tao, S.; Zhang, X. Y.; Gao, Z. Y.; Chen, T. Y.; Min, H. H.; Yang, H.; Chen, H. Y.; Shen, X. D.; Wang, J.; Yang, H. Dynamic electronic and ionic transport actuated by cobalt-doped $MoSe_2$/rGO for superior potassium-ion batteries. *Small* **2023**, *19*, 2304200.

[39] Genorio, B.; Lu, W.; Dimiev, A. M.; Zhu, Y.; Raji, A. R. O.; Novosel, B.; Alemany, L. B.; Tour, J. M. *In situ* intercalation replacement and selective functionalization of graphene nanoribbon stacks. *ACS Nano* **2012**, *6*, 4231–4240.

[40] Wang, T.; Wang, Z.; Salvatierra, R. V.; Mchugh, E.; Tour, J. M. Top-down synthesis of graphene nanoribbons using different sources of carbon nanotubes. *Carbon* **2020**, *158*, 615–623.

[41] Cui, L. F.; Wang, Z. D.; Kang, S. F.; Fang, Y. Y.; Chen, Y.; Gao, W. K.; Zhang, Z. Y.; Gao, X.; Song, C. Y.; Chen, X. D. et al. N, P codoped hollow carbon nanospheres decorated with $MoSe_2$ ultrathin nanosheets for efficient potassium-ion storage. *ACS Appl. Mater. Interfaces* **2022**, *14*, 12551–12561.

[42] Liu, Y. L.; Zhai, Y. J.; Wang, N. N.; Zhang, Y. H.; Lu, Z. X.; Xue, P.; Bai, L.; Guo, M. Q.; Huang, D.; Bai, Z. C. Ultrathin $MoSe_2$ nanosheets confined in N-doped macroporous carbon frame for enhanced potassium ion storage. *ChemistrySelect* **2020**, *5*, 2412–2418.

[43] Yu, L.; Wang, G. R.; Gao, J. Y.; Li, J.; Peng, B.; Zhang, G. Q. Sacrificial nanowire catalyzed polymerization process generates hierarchical $MoSe_2$ grafted carbonaceous nanotubes for superior potassium ion storage. *ACS Appl. Energy Mater.* **2021**, *4*, 6757–6767.

[44] Kang, W. P.; Wang, Y. Y.; Xu, J. Recent progress in layered metal dichalcogenide nanostructures as electrodes for high-performance sodium-ion batteries. *J. Mater. Chem. A* **2017**, *5*, 7667–7690.

[45] Zhu, Y. R.; Li, J. Y.; Yun, X. R.; Zhao, G. G.; Ge, P.; Zou, G. Q.; Liu, Y.; Hou, H. S.; Ji, X. B. Graphitic carbon quantum dots modified nickel cobalt sulfide as cathode materials for alkaline aqueous batteries. *Nano-Micro Lett.* **2020**, *12*, 16.

[46] Liu, H.; Guo, H.; Liu, B. H.; Liang, M. F.; Lv, Z. L.; Adair, K. R.; Sun, X. L. Few-layer $MoSe_2$ nanosheets with expanded (002) planes confined in hollow carbon nanospheres for ultrahigh-performance Na-ion batteries. *Adv. Funct. Mater.* **2018**, *28*, 1707480.

[47] Yi, Y. Y.; Sun, Z. T.; Li, C.; Tian, Z. N.; Lu, C.; Shao, Y. L.; Li, J.; Sun, J. Y.; Liu, Z. F. Designing 3D biomorphic nitrogen-doped $MoSe_2$/graphene composites toward high-performance potassium-ion capacitors. *Adv. Funct. Mater.* **2020**, *30*, 1903878.

[48] Wang, Z. D.; Gao, W. K.; Ding, C. J.; Qi, H. Y.; Kang, S. F.; Cui, L. F. Boosting potassium-ion storage in large-diameter carbon nanotubes/MoP hybrid. *J. Colloid Interface Sci.* **2021**, *584*, 875–884.

[49] Shen, Q.; Jiang, P. J.; He, H. C.; Chen, C. M.; Liu, Y.; Zhang, M. Encapsulation of $MoSe_2$ in carbon fibers as anodes for potassium ion batteries and nonaqueous battery-supercapacitor hybrid devices. *Nanoscale* **2019**, *11*, 13511–13520.

[50] Teng, Y. Q.; Zhao, H. L.; Zhang, Z. J.; Li, Z. L.; Xia, Q.; Zhang, Y.; Zhao, L. N.; Du, X. F.; Du, Z. H.; Lv, P. P. et al. MoS_2 nanosheets vertically grown on graphene sheets for lithium-ion battery anodes. *ACS Nano* **2016**, *10*, 8526–8535.

[51] Zheng, F. H.; Zhong, W. T.; Deng, Q.; Pan, Q. C.; Ou, X.; Liu, Y. Z.; Xiong, X. H.; Yang, C. H.; Chen, Y.; Liu, M. L. Three-dimensional (3D) flower-like $MoSe_2$/N-doped carbon composite as a long-life and high-rate anode material for sodium-ion batteries. *Chem. Eng. J.* **2019**, *357*, 226–236.

[52] Wang, W.; Jiang, B.; Qian, C.; Lv, F.; Feng, J. R.; Zhou, J. H.; Wang, K.; Yang, C.; Yang, Y.; Guo, S. J. Pistachio-shuck-like $MoSe_2$/C core/shell nanostructures for high-performance potassium-ion storage. *Adv. Mater.* **2018**, *30*, 1801812.

[53] Niu, F. E.; Yang, J.; Wang, N. N.; Zhang, D. P.; Fan, W. L.; Yang, J.; Qian, Y. T. $MoSe_2$-covered N,P-doped carbon nanosheets as a long-life and high-rate anode material for sodium-ion batteries. *Adv. Funct. Mater.* **2017**, *27*, 1700522.

[54] Xu, D.; Chen, L.; Su, X. Z.; Jiang, H. L.; Lian, C.; Liu, H. L.; Chen, L.; Hu, Y. J.; Jiang, H.; Li, C. Z. Heterogeneous $MoSe_2$/nitrogen-doped-carbon nanoarrays: Engineering atomic interface for potassium-ion storage. *Adv. Funct. Mater.* **2022**, *32*, 2110223.

[55] Zhao, Z. C.; Hu, Z. Q.; Liang, H. Y.; Li, S. D.; Wang, H. T.; Gao, F.; Sang, X. C.; Li, H. S. Nanosized $MoSe_2$@carbon matrix: A stable host material for the highly reversible storage of potassium and aluminum ions. *ACS Appl. Mater. Interfaces* **2019**, *11*, 44333–44341.

[56] Li, N. N.; Sun, L.; Wang, K.; Zhang, J.; Liu, X. H. Anchoring $MoSe_2$ nanosheets on N-doped carbon nanotubes as high performance anodes for potassium-ion batteries. *Electrochim. Acta* **2020**, *360*, 136983.

[57] Zhang, X. Q.; Xiong, Y. L.; Zhang, L.; Hou, Z. G.; Qian, Y. T. Hierarchical interlayer-expanded $MoSe_2$/N–C nanorods for high-rate and long-life sodium and potassium-ion batteries. *Inorg. Chem. Front.* **2021**, *8*, 1271–1278.

Jiamei Liu received her master degree from Nanjing Normal University in 2006. He now works at the Core Facilities and Experiment Center of Xi'an Jiaotong University. Her current scientific interests focus on energy storage materials, and *in-situ* characterization techniques.

Xiaowei Shi received her master degree from the school of Materials Science and Engineering, Xi'an Jiaotong University, China, in 2015. She received her Ph.D. degree in Xi'an Jiaotong University. Her major research focus is on energy storage materials and devices, including corrosion in Li-ion batteries, and dendrite suppression of Li metal anode.

Jia Liu received her Ph.D. degree in Physical Chemistry (2021) from Xiamen University (XMU) She now works as an engineer in Instrumental Analysis Center in Xi'an Jiaotong University, Xi'an, PR China. Her research interests focus on electrochemical *in-situ* Raman spectroscopic study, *in situ* Infrared Spectroscopic study, transient absorption, and plasmonic photo-electrocatalysis.

Chang Huang received his master degree from School of Physics from Xi'an Jiaotong University in 2010. He now works at the Core Facilities and Experiment Center of Xi'an Jiaotong University. His current scientific interests focus on X-ray diffraction and small angle X-ray scattering.

Chao Li received his bachelor's degree from Shijiazhuang Tiedao University in 2022. He is currently pursuing a master's degree in the School of Chemistry at Xi'an Jiaotong University. His research interests are mainly focused on the performance improvement of PVDF-HFP based polymer solid state batteries.

Haixiao Kang received his Bachelor of Engineering degree from the Faculty of Environmental Science and Engineering in Kunming University of Science and Technology in 2005, and his Ph.D. degree from the School of Environmental and Municipal Engineering in Lanzhou Jiaotong University in 2020. He is currently an associate professor at College of Geography and Environment Sciences, Baoji University of Arts and Sciences. His research interests focus on the preparation and application of functional materials.

Zhan Gao received his Ph.D. degree in Materials Science from the KTH Royal Institute of Technology in Sweden in 2011. He continued his postdoctoral research at Department of Materials Science and Engineering in Northwestern University till 2016. After working in Plastic Onnium company as a research engineer for several years, he joined School of Chemical Engineering and Technology as a full professor and group leader at Xi'an Jiaotong University. His research interests mainly include development of high-performance reversible solid oxide cells for energy storage, novel anode materials for hydrocarbonous fuels, electrochemical characterization and identification of reaction mechanisms of SOFC electrodes and low carbon hydrogen production by reforming technologies.

Lei Li received his M.S. and Ph.D. degrees in Chemistry from Jilin University and Rice University in 2010 and 2015, respectively. After his postdoctoral research at Department of Materials Science and Engineering in Northwestern University, he joined School of Materials Science and Engineering as a full professor at Xi'an Jiaotong University. He is leading a group that mainly studies the materials and device performance in energy conversion and storage.